Cloud top phase distributions of simulated deep convective clouds

C. Hoose[1,*], M. Karrer[1,*], C. Barthlott[1]

[1]Karlsruhe Institute of Technology, Institute of Meteorology and Climate Research, Karlsruhe, Germany

Key Points:

- Cloud top phase distributions of deep convective clouds differ systematically from in-cloud phase distributions.
- The phase distributions contain fingerprints of primary and secondary ice formation processes.
- Coarse-graining and co-variation of the cloud dynamics diminish these fingerprints of microphysical processes.

*These authors contributed equally to the manuscript.

Corresponding author: Corinna Hoose, corinna.hoose@kit.edu

Abstract

Space-based observations of the thermodynamic cloud phase are frequently used for the analysis of aerosol indirect effects and other regional and temporal trends of cloud properties; yet, they are mostly limited to the cloud top layers. This study addresses the information content in cloud top phase distributions of deep convective clouds during their growing stage. A cloud-resolving model with grid spacings of 300 m and lower is used in two different setups, simulating idealized and semi-idealized isolated convective clouds of different strengths. It is found that the cloud top phase distribution is systematically shifted to higher temperatures compared to the in-cloud phase distribution due to lower vertical velocities and a resultingly stronger Wegener-Bergeron-Findeisen process at the cloud top. Sensitivity studies show that heterogeneous freezing can modify the cloud top glaciation temperature (where the ice pixel fraction reaches 50%), and ice multiplication via rime splintering is visible in an early ice onset at temperatures around $-10°$C. However, if the analyses are repeated with a coarsened horizontal resolution (above 1 km, similar to many satellite datasets), a significant part of this signal is lost, which limits the detectability of these microphysical fingerprints in the observable cloud top phase distribution. In addition, variation in the cloud dynamics also impacts the cloud phase distribution, but cannot be quantified easily.

1 Introduction

At temperatures between 0 and approximately $-37°$C, atmospheric hydrometeors can occur both in the liquid and in the ice phase. The liquid phase is metastable in this temperature range, while the more stable ice phase forms through homogeneous or heterogeneous ice nucleation (including collisional contact with other ice crystals) and - once the first ice is present - growth from the vapour phase [*Lamb and Verlinde*, 2011]. As this can lead to rapid formation of hydrometeors with significant fall velocities through the Wegener-Bergeron-Findeisen process [*Findeisen*, 1938; *Storelvmo and Tan*, 2015], most precipitation on Earth, in particular over continents, stems from clouds with mixed-phase or ice tops [*Mülmenstädt et al.*, 2015]. Furthermore, the radiative effects of liquid and ice clouds differ due to changes in hydrometeor size distributions and scattering properties [*Petty*, 2004; *Liou*, 1981] as well as differences in the typical cloud altitude, thickness and lifetime. Thus, liquid, mixed-phase and ice clouds have distinct effects on the surface and top-of-the-atmosphere radiative budgets [*Matus and L'Ecuyer*, 2017; *Cesana and Storelvmo*, 2017]. Anthropogenic disturbances can impact the phase partitioning in clouds through microphysical and thermodynamic effects, with implications for the effective radiative forcing and equilibrium climate sensitivity [*Lohmann*, 2017; *Storelvmo*, 2017].

Observations of the cloud phase distribution reveal a strong dependency on temperature, but also on other factors, such as the cloud type. Furthermore, the results depend on the methods used to discriminate ice and liquid and on averaging scales. In-situ aircraft observations within stratiform clouds showed that the local cloud phase structure is mostly uniform on scales of 100 m [*Korolev et al.*, 2003; *Mazin*, 2006]. Already at temperatures just below 0°C, the frequency of purely liquid clouds derived from these observations is substantially lower than 1. This early ice onset is less pronounced in observations with ground-based lidar [*Seifert et al.*, 2010; *Kanitz et al.*, 2011], possibly because only ice precipitating clouds can be identified as mixed-phased with this method. Aircraft-based remote sensing of the vertical phase profile in convective clouds, seen from the side, has shown promising first results [*Martins et al.*, 2011; *Jäkel et al.*, 2017], but no data set large enough for statistical analysis is available from this method yet.

Satellite observations with active sensors (CALIOP (Cloud-Aerosol Lidar with Orthogonal Polarization) and CloudSat) [*Choi et al.*, 2010a; *Hu et al.*, 2010; *Tan et al.*, 2014; *Zhang et al.*, 2015; *Cesana et al.*, 2016; *Kikuchi et al.*, 2017] provide (in spite of a sparse coverage) a global picture of the cloud phase distribution, and are valuable for the evaluation of global climate models [*Komurcu et al.*, 2014; *Cesana et al.*, 2015]. CALIOP yields information on the vertical phase distribution within the cloud up to saturation of the lidar signal (at an optical thickness of approximately 5) [*Winker et al.*, 2010]. Cloud phase products from passive sensors like MODIS (Moderate Resolution Imaging Spectroradiometer) [*Naud et al.*, 2006; *Choi et al.*, 2010b; *Morrison et al.*, 2011], POLDER (POLarization and Directionality of the EarthâĂŹs Reflectances) [*Weidle and Wernli*, 2008], AIRS (Atmospheric Infrared Sounder) [*Naud and Kahn*, 2015] and AVHRR (Advanced Very High Resolution Radiometer) [*Carro-Calvo et al.*, 2016] have a better coverage of the globe due to wider swaths and provide better statistics, allowing also for detailed studies of specific cloud regimes. However, the retrieved cloud phase refers to the cloud top only. *Yuan et al.* [2010] proposed a method to derive vertical profiles of the cloud phase for larger cloud systems by analysing the effective radius at different cloud top temperatures within the ensemble. This method was successfully applied to deep convective cloud clusters [*Rosenfeld et al.*, 2011].

Deep convective clouds are usually mixed-phase clouds with liquid layers at the bottom and ice at the cloud top, which is in most cases below $-37°C$. However, while deep convective clouds evolve from a relatively low cloud base and rise to higher levels (cumulus stage), the cloud top can still be to a large part liquid (*cumulus congestus* or *cumulonimbus calvus*) with only moderate ice contents, and its contours are still well defined. Only in the mature stage (*cumulonimbus incus* or *cumulonimbus capillatus*) a dense anvil of pure ice spreads at the cloud top [*Houze*, 1993]. *Zipser* [2003] argued that for tropical hot towers, which undergo substantial dilution by entrainment, the additional latent heat release during ice formation is crucial to provide enough buoyancy for an ascent to the tropical tropopause. It is this stage of ice formation at the cloud top during the growth phase of a deep convective cloud that this study focusses on. Deep convective clouds are most frequent over tropical, subtropical and midlatitude continents in summer as well as over the tropical oceans [*Yuan and Li*, 2010; *Peng et al.*, 2014]. Numerical modelling has indicated that the glaciation of these clouds is at least to some extent sensitive to the concentration of ice nucleating particles [*Connolly et al.*, 2006; *van den Heever et al.*, 2006; *Ekman et al.*, 2007; *Fan et al.*, 2010; *Hiron and Flossmann*, 2015; *Paukert et al.*, 2017], but most studies have focussed on the variation of aerosols acting as cloud condensation nuclei [see the reviews by *Tao et al.*, 2012; *Fan et al.*, 2016], and resulting effects on warm phase microphysical processes, dynamical invigoration and precipitation at the ground.

In this study, we address the question in how far the cloud top phase distribution of deep convective clouds (as retrieved from passive satellite sensors) differs from the in-cloud phase distribution and what parameters and microphysical processes it depends on. To this end, we use idealized and semi-idealized high-resolution simulations. Deep convective clouds were chosen because their cloud tops transition the entire mixed-phase cloud temperature range during the growing phase of the cloud.

In section 2, the model simulations and the analysis methods are described. In section 3, the results are shown and discussed. In the conclusions, implications for the interpretation of cloud phase observed from space are discussed.

2 Methods

2.1 Model description

The nonhydrostatic limited-area model of the Consortium for Small-Scale Modelling (COSMO) [*Baldauf et al.*, 2011], version 5.0, was used in a research configuration in this study. As the model is employed at grid spacings below 1 km, no convection parameterization nor subgrid cloud scheme are used. The two-moment microphysics scheme [*Seifert and Beheng*, 2006; *Seifert et al.*, 2012] includes six hydrometeor categories (cloud droplets, rain, ice crystals, snow, graupel and hail). A saturation adjustment scheme is employed for condensation and evaporation of liquid condensate down to a temperature of 233 K, while depositional growth and sublimation of ice are parameterized as time-dependent processes. Cloud condensation nuclei (CCN) activation is calculated according to *Segal and Khain* [2006] under the assumption of a continental CCN spectrum. Primary ice formation is included with a combined parameterization of deposition nucleation and condensation freezing and a separate treatment of immersion freezing of rain drops. Deposition nucleation and condensation freezing is formulated as a relaxation to a temperature- and ice supersaturation-dependent ice nucleating particle (INP) concentration N_{INP} [*Murakami*, 1990; *Reisner et al.*, 1998]:

$$N_{INP} = N_0 \left(\frac{e/e_{sat,i}}{\mathrm{MAX}(e_{sat,w}/e_{sat,i}, 1.001) - 1} \right)^{4.5} \cdot \exp\left(-k_T \cdot \mathrm{MAX}(T_C, -27.15)\right) \quad (1)$$

$$\Delta N_i = \mathrm{MAX}\left(N_{INP} - (N_i + N_s), 0\right) \quad (2)$$

Here, e is the water vapor pressure, $e_{sat,i}$ the saturation vapor pressure with respect to ice, $e_{sat,i}$ the saturation vapor pressure with respect to liquid water, T_C the temperature in °C and the constants are $N_0 = 0.01\ \mathrm{m}^{-3}$ and $k_T = 0.6\,{}^\circ\mathrm{C}^{-1}$. N_i and N_s are the prognostic number concentrations of ice crystals and snow. ΔN_i is the change in N_i due to deposition and immersion ice nucleation within one model timestep. The parameterization is applied for all gridpoints with $T_C < 0$°C and $e > e_{sat,i}$. At water saturation, this parameterization has a somewhat stronger temperature dependence then typical observed ice nucleating particle concentrations [*DeMott et al.*, 2010], with values around $10^2\ \mathrm{m}^{-3}$ at $-15\,$°C (which is at the lower end of the observed range) and a maximum of $1.2 \times 10^5\ \mathrm{m}^{-3}$ for $T_C \leq -27.15\,$°C (only observed in dust-laden air masses).

Rain drop freezing is parameterized as a time-, temperature- and volume-dependent process, assuming that the probability of the presence of an ice nucleating particle in the droplet increases proportionally to the droplet volume [*Bigg*, 1953]. Recent model improvements to harmonize freezing of cloud droplets and rain drops and to treat both as aerosol-dependent processes [*Paukert et al.*, 2017] are not included in this study. Homogeneous freezing of cloud drops is parameterized following *Cotton and Field* [2002] for temperatures below $-30°$C.

Secondary ice formation is included for the rime-splintering process proposed by *Hallett and Mossop* [1974].

$$\Delta N_i = C_{HM}\Delta q_{rim}\mathrm{MAX}\left(1, \mathrm{MIN}\left(0, \frac{T-265}{268-265}\right)\right)\mathrm{MAX}\left(1, \mathrm{MIN}\left(0, \frac{270-T}{270-268}\right)\right) \quad (3)$$

with $C_{HM} = 3.5 \cdot 10^8$ kg^{-1}, the rimed condensate mass Δq_{rim} and temperature T in K. Riming is allowed between cloud droplets of a minimum mean diameter of 10 μm and ice crystals, snow particles (both with a minimum diameter of 150 μm), graupel and hail (both with a minimum diameter of 100 μm), and between rain drops (without further size restriction) and ice crystals, snow particles (again with minimum diameters of 150 μm), graupel and hail (without size restriction). Other potential ice multiplication processes [*Field et al.*, 2017; *Sullivan et al.*] are not included.

2.2 Setup of the simulated cases

Two simulation setups for deep convective clouds are used in this study. The first one is a highly idealized setup with convection triggered by a warm bubble over flat terrain, following *Weisman and Klemp* [1982] and *Weisman and Rotunno* [2000]. The initial thermodynamic profile has a low-level water vapor mixing ratio of 14 g/kg and a convective available potential energy (CAPE) of 2200 J/kg. For the background flow, a quarter-circle shear profile to 2 km above ground level with unidirectional shear above (up to a maximum horizontal wind speed of 31 m/s at 6 km above ground level, with constant wind above) was used. A temperature disturbance of 2 K , with a radius of 10 km, was placed in the south west corner of the domain (60 km distance from the domain boundaries) at an altitude of 1.4 km. The model resolution used for this case is 300 m, with 1000×800 horizontal grid cells, and 64 vertical levels. Similar simulations with the COSMO model were presented e. g. by *Zeng et al.* [2016]; *Paukert et al.* [2017]; *Hande and Hoose* [2017].

The second setup is semi-idealized, with realistic topography and an initial temperature and humidity profile (CAPE of 774 J/kg) from radiosoundings near Jülich, Germany [*Hande et al.*, 2017; *Hande and Hoose*, 2017]. The initial wind profile is taken from *Weisman and Klemp* [1982] (unidirectional shear of 5 m/s, with a wind direction of 225°), and the boundary conditions are fixed. Convection is triggered by local convergence in the flow over the orographically structured terrain. The solar insolation is kept constant corresponding to the position of the sun at 12 p.m. local time. The horizontal resolution for this simulation is approximately 110 m, with 600 $\times$ 600 horizontal grid cells, and 100 vertical levels. For this setup, a small ensemble of three members is generated by increasing either the near-surface temperature or the dew point temperature in the boundary layer by 2 K.

2.3 Diagnostics

In the following, cloud top conditions are compared to those within the cloud. The definition of "cloud top" employed in this study is designed to mimic the capability of passive satellite sensors, which receive signals only from the uppermost layers of a cloud. Different approaches have been followed in the literature. As an example, *Weidle and Wernli* [2008], in order to extract a dataset comparable to POLDER-1 observations, integrated the ice and liquid mass concentrations up to a minimum cloud water path of 10 g/m^2, which is roughly equivalent to an optical thickness of 3 (coinciding with the threshold for reliable cloud detection by POLDER-1 [*Chepfer et al.*, 2000]). Here, we follow the approach by *Pincus et al.* [2012]. For a MODIS satellite simulator of the cloud phase, they suggested to average the cloud phase, weighted by the extinction due to liquid and ice particles, levelwise from the uppermost cloud layer up to an optical depth of 1. Similarly, we calculate the cloud top liquid fraction lf_{CT} by

$$lf_{CT} = \frac{1}{\tau_{lim}} \int_0^{\tau_{lim}} lf(z)(\beta_{e,c} + \beta_{e,i})(z)dz. \tag{4}$$

Here, $\beta_{e,c}$ and $\beta_{e,i}$ are the shortwave extinction coefficients of the liquid and ice hydrometeors, and $lf(z)$ is the levelwise liquid mass fraction ($lf = q_c/(q_c+q_i)$), with the mixing ratios of cloud droplets q_c and of ice crystals q_i. Large hydrometeors (rain, snow, graupel and hail) are not included in lf because of their relatively small contribution to the optical extinction. Similarly, the cloud top temperature lf_{CT} is obtained as follows:

$$T_{CT} = \frac{1}{\tau_{lim}} \int_0^{\tau_{lim}} T(z)(\beta_{e,c} + \beta_{e,i})(z)dz. \tag{5}$$

While *Pincus et al.* [2012] suggested a threshold optical depth τ_{lim} of 1 for the MODIS simulator, we use here $\tau_{lim} = 0.2$. For this threshold optical depth, the highest Hanssen-Kuiper skill score was found in a comparison of the CLAAS-2 (CLoud property dAtAset using SEVIRI, Edition 2) cloud phase product (derived from geostationary Meteosat Spinning Enhanced Visible and Infrared Imager (SEVIRI) measurements) and CALIOP [*Benas et al.*, 2017].

The glaciation temperature T_{50}, i. e. the temperature at which $lf = 0.5$ is reached, is diagnosed here in the following way: In temperature intervals of 1 K, the mean lf ($\overline{lf}(T)$) is calculated for all mixed-phase pixels, i. e. pixels at which $\epsilon < lf < 1 - \epsilon$ ($\epsilon = 10^{-4}$). To exclude pixels with very low amounts of cloud condensate, only those pixels with an extinction coefficient $\beta_{e,c} + \beta_{e,i}$ larger than 0.002 m^{-1} within the cloud (with a layer thickness of 100 m, this corresponds to an optical thickness of 0.2) are included. For the cloud top analysis (lf_{CT}), only cloud top pixels with an optical depth larger than 0.2 are included. The glaciation temperature is then interpolated linearly between the neighbouring temperature bins encompassing $\overline{lf} = 0.5$. If $\overline{lf}$ does not decrease monotonically with decreasing temperature, the highest temperature with $\overline{lf} \geq 0.5$ is chosen.

As retrieval schemes for passive satellite sensors, e.g. *Pavolonis et al.* [2005], provide a binary distinction into liquid or ice clouds (a mixed-phase cloud type is often defined, but not used), we also define a binary liquid cloud top fraction blf, which is given by the number (N) of liquid pixels divided by the total number of cloudy pixels. As liquid pixels, we define all pixels with a cloud top liquid mass fraction larger than 0.5, mimicking a perfect satellite retrieval.

$$blf(T_{CT}) = \frac{N(lf_{CT}(T_{CT}) > 0.5)}{N(lf_{CT}(T_{CT}) > 0.5) + N(lf_{CT}(T_{CT}) \leq 0.5)} \tag{6}$$

blf is thus defined as one value for each value (or bin) of cloud top temperature T_{CT}, sampling all pixels throughout the cloud evolution.

3 Results

3.1 Cloud cross sections

Fig. 1 illustrates the vertical structure in the simulated clouds at a mature convective stage, after approximately 3 hours into the simulation. Both clouds exhibit a warm cloud base, a mainly liquid updraft core, a narrow region of mixed phase and a large ice anvil. The cloud is much smaller in the semi-idealized simulation and the anvil does not reach as high as in the warm bubble setup. Therefore, the outflow also still contains some pockets with liquid water (Fig. 1(d)). As expected from the higher CAPE, the maximum updraft is larger with 30 $\mathrm{m\,s^{-1}}$ in the warm bubble case as in the semi-idealized case with 15 m/s. The extinction coefficient is highest within the main updraft in both cases (values of approximately 0.5 $\mathrm{m^{-1}}$), but reaches its maximum at lower levels in the warm bubble simulation. In the pure ice region directly above the updraft, values are below 0.01 $\mathrm{m^{-1}}$ (Fig. 1(e) and (f)), and in the anvil in the warm bubble case in larger distance from the updraft core, below 0.001 $\mathrm{m^{-1}}$, in agreement with observational and modelling studies [e. g., *Garrett et al.*, 2005; *Fan et al.*, 2010]. Also regions of falling ice at lower levels exhibit low extinction coefficients below 0.001 $\mathrm{m^{-1}}$. The uppermost layer of the cloud, wherever below 0°C, is always a mixed-phase or ice layer with a low extinction coefficient. Overlayed on the plots in the second row of Fig. 1 is a black line indicating where an optical depth of 0.2 is reached, when integrating from cloud top downwards. The ice-containing layer at cloud top often has an optical depth lower than 0.2, such that an integration as in Eq. (4) leads to an averaging of this layer with lower layers, which have a higher liquid mass fraction.

3.2 In-cloud and cloud top liquid mass fractions

As a first diagnostic, the in-cloud liquid mass fraction lf is analysed. The liquid fraction, sampled at intervals of 6 minutes from all cloudy gridpoints with a minimum extinction coefficient of 0.002 $\mathrm{m^{-1}}$, is shown as scatterplot versus the pixel temperature in Fig. 2 (a) and (c) for the warm bubble simulations and in Fig. 2 (b) and (d) for the semi-idealized simulations. The data points are colorcoded by the vertical velocity in Fig. 2 (a) and (b) and by the liquid plus ice cloud condensate mass mixing ratio in Fig. 2 (c) and (d). The relative frequency of occurrence of the points is shown in Fig. 2 (e) and (f). In both model setups, in-cloud liquid fractions smaller than 0.9 are common already at temperatures lower than ≈ -2°C, while they approach 0 only below -30°C. At the lower end of the mixed-phase temperature range, a clear tendency of higher lf with higher vertical velocity becomes apparent, which is probably due to the suppression of the Wegener-Bergeron-Findeisen process in strong updrafts, where the supersaturation with respect to water is maintained. This interpretation is also supported by the trend to higher condensate mixing ratios at these pixels, in particular in the semi-idealized setup (Fig. 2 (d)). We assume that the condensate mass is generally high in regions of strong condensation/depositional growth and low in regions of evaporation/sublimation, although no perfect correlation with the condensation rate is expected due to accumulation over time, advection, sedimentation and other loss processes. These confounding factors might contribute to the small values of condensate mass in the regions of strong updraft and high lf at the low temperature end for the warm bubble case (Fig. 2 (c)). Low values of lf occur also at temperatures between ≈ -4 and ≈ -12°C in regions with low upward vertical velocities or downdrafts. As shown later, these are caused by ice multiplication via rime splintering, and are presumably enhanced by the Wegener-Bergeron-Findeisen process.

Next, the cloud top liquid mass fraction lf_{CT} is plotted against the cloud top temperature T_{CT} (Fig. 2 (g) and (h)), both calculated as a weighted average over the topmost cloud layers until an optical depth of 0.2 is reached (Eq. (4)). The cloud top phase distribution is generally characterized by more pixels with intermediate values of lf_{CT}. This and also the higher frequency of pixels along a diagonal straight line (seen in the histograms in Fig. 2 (i) and (j)) can be explained by the averaging of cold, pure ice layers and warmer, liquid in-cloud layers.

It is also apparent from Fig. 2 (g) and (h) that at cloud top, the vertical velocities are significantly smaller as within the cloud. Therefore, in-situ ice formation through the Wegener-Bergeron-Findeisen process is expected to be more efficient. Thus, at a given temperature lower than ≈ -20°C, the cloud top liquid fraction is typically lower at the cloud top than within the cloud. An exception are values of $lf_{CT} \leq 0.3$ for $T_{CT} \leq -35$°C, which are rare at in-cloud pixels (Fig. 2 (a) and (b)), but appear more often in the cloud top diagnostic (Fig. 2 (g) and (h)), again as a result of averaging. The shift to lower liquid fractions due to the more active Wegener-Bergeron-Findeisen process results also in a shift of the diagnosed glaciation temperature, which is also indicated in Fig. 2 for both in-cloud and cloud top pixels in both simulation setups. In the warm bubble case, T_{50} shifts from -28.6°C (in-cloud) to -26.4°C (cloud top), while in the semi-idealized setup, the shift is even larger (-29.3°C (in-cloud) versus -22.8°C (cloud top)).

3.3 Liquid cloud top pixel number fraction and resolution effect

Also from data throughout the entire simulation period, the binary liquid cloud top pixel number fraction blf (Eq. (6)) is binned into cloud top temperature intervals of 2 K and shown in Fig. 3 as black lines. Comparing the temperature where blf reaches 0.5 to T_{50} derived from the cloud top liquid mass fraction (Fig. 2 (g) and (h)), $T(blf = 0.5)$ is for both simulations higher than T_{50}, by about 2°C for the warm bubble simulation and by about 1°C for the semi-idealized simulation. This is because T_{50} refers to mixed-phase pixels only (with the intention to define a diagnostic related to the glaciation process), and pure ice pixels excluded for its calculation, while $T(blf = 0.5)$ is an integral variable also including those gridpoints where no liquid water is or has ever been present. It is also apparent in Fig. 3 that $blf(T)$ is not symmetric: it approaches $blf = 0$ much faster than $blf = 1$.

When the model output is averaged to coarser grids (combining 2×2, 5×5, 8×8 and 10×10 pixels into one mean value) before calculating cloud top values and blf, two effects can be observed in $blf(T)$: the curves shift to lower temperatures (by several °C), and they become more symmetric because with coarser resolution, they converge towards $blf = 1$ at temperatures above ≈ -15°C. As predominantly ice pixels generally have lower optical depths and lower condensate masses than predominantly liquid pixels, their number is reduced disproportionally during the coarse graining, which involves averaging of adjacent pixels weighted by the condensate mass. This effect is expected to be most pronounced for homogeneous mixtures of ice and liquid cloud pixels. However, the shift of the curves in Fig. 3 is not monotonic, because these conditions (homogeneous mixtures, higher condensate masses in liquid cloud pixels) are not always fulfilled and because sample size is limited.

3.4 Sensitivity studies: impact of ice multiplication, heterogeneous freezing and the thermodynamic profile

Eight sensitivity experiments were run for the semi-idealized setup: switching off ice multiplication (i. e., disabling Eq. (3)); scaling heterogeneous ice formation by multiplying N_0 in Eq. (1) by 0.01, 0.1, 10, 100 and 1000; and changes to the thermodynamic profile by increasing either the near-surface temperature or the dewpoint temperature in the boundary layer by 2 K each. The latter two modifications lead to an increase in CAPE from 774 to 1265 and 1889 J kg^{-1} and lead therefore to significantly more vigorous convection.

The results for the in-cloud liquid mass fraction (for the simulations without ice multiplication and with $N_0 \times 1000$) are displayed in Fig. 4. Without ice multiplication, all values of an in-cloud liquid mass fraction smaller than 0.6 at temperatures above -15°C disappear (Fig. 4(a)). This also results in an increase in the liquid cloud top pixel number fraction blf to values above 0.9 in the same temperature range (Fig. 5(a)). The increase of heterogeneous INP, by contrast, mostly affects the in-cloud liquid mass fraction at temperatures below -15°C (Fig. 4(b)), and the glaciation temperatures (T_{50} and $T(blf = 0.5)$) shift by several K as a function of N_0 (see again Fig. 5(a)). Interestingly, lower values of N_0 only result in small changes, and the simulations with $N_0 \times 0.01$ and $N_0 \times 0.1$ do not differ significantly. This is probably due to rain drop freezing, which is parameterized independent of N_0, becoming the dominant primary ice formation process in these simulations. In contrast, increases in N_0 lead to a monotonic and strong shift of $T(blf = 0.5)$.

Fig. 5(b) illustrates the effect of coarse graining on these features. As discussed in section 3.3, averaging to a coarser grid results in a shift of the glaciation temperature to lower values and in a more symmetric behavior of $blf(T)$. Compared to the effect of an increase of INP by two orders of magnitude, the effect of the averaging is small, and the difference in glaciation temperature between the control simulation and the simulation with $N_0 \times 1000$ remains very similar. In contrast, the signal of the early ice onset caused by ice multiplication becomes weaker on a coarser resolution, to the extent that the shapes of the curves are nearly identical when analyzed on a 1.1 km grid.

The changes to the thermodynamic profile, despite significantly higher CAPE and resulting higher vertical velocities inside the cloud (not shown), lead only to small changes in the binary liquid cloud top pixel number fraction (Fig. 5(c)). Interestingly, the cloud top glaciation temperature $T(blf = 0.5)$ increases slightly in both sensitivity experiments, which seems to contradict the earlier finding that higher vertical velocities induce a lower glaciation temperature. This is because cloud top vertical velocities are small anyway (see Fig. 2(e) and (f)) and do not change substantially in the sensitivity experiments (not shown). So the difference in cloud top phase between the warm bubble and semi-idealized simulations seem to be mainly due to differences in cloud structure and organization, not directly due to the different convective strength. Overall, the impact of these modifications to the thermodynamic profile on the cloud phase distribution are much smaller than the impact of the changes to primary and secondary ice formation parameterizations.

4 Discussion and conclusions

In our analysis of the phase distribution within and at the top of convective clouds based on two different setups with the COSMO model, the following features are apparent:

- In the in-cloud phase distribution, we see a strong signature of vertical velocity. Physically, this can be explained by the suppression of the Wegener-Bergeron-Findeisen process in strong enough updrafts [*Korolev*, 2007]. As the microphysics scheme employed here [*Seifert and Beheng*, 2006] includes a saturation adjustment scheme for condensation and evaporation of liquid condensate, the dependence of the Wegener-Bergeron-Findeisen process on updraft velocity is only represented in a simplified manner, namely by the suppression of evaporation if the updraft is strong enough to maintain supersaturation with respect to liquid water. It would be interesting to study this effect in a model with a prognostic treatment of supersaturation [e.g., *Morrison and Grabowski*, 2008].

- Mainly due to this vertical velocity signal, we find a systematic bias of the cloud top phase distribution compared to the in-cloud phase distribution. This has implications for the signal received by space-based passive remote sensing instruments. The maximum vertical velocities occur within the cloud, while the simulated cloud top regions are dominated by smaller vertical velocities and thus lower liquid mass fractions at a given temperature. The cloud top glaciation temperature is therefore systematically higher than an equivalent in-cloud glaciation temperature. In the available global climatological studies of the supercooled liquid fraction or the cloud glaciation temperature, this shift is not seen: While *Carro-Calvo et al.* [2016] report cloud top glaciation temperatures around -25 to $-30°$C based on an analysis of AVHRR observations, several studies based on CALIOP measurements (penetrating into the clouds at least to some extent) find supercooled liquid cloud fractions of 50% at temperatures between -15 and $-25°$C [*Hu et al.*, 2010; *Choi et al.*, 2010a; *Komurcu et al.*, 2014]. This discrepancy could be due to the fact that also CALIOP can not detect phase changes in convective clouds because of a saturation of the lidar signal, and the expected effect is smaller for optically less dense clouds. Additionally, uncertainties remain in both the phase retrieval and the cloud top temperature retrieval from passive sensors [*Taylor et al.*, 2017].
- Heterogeneous ice nucleation significantly influences the cloud phase distribution during the cumulus stage of the simulated convective clouds, and determines the derived glaciation temperature, even if the clouds eventually reach temperatures at which homogeneus freezing dominates. This finding is in agreement with previous studies. Such an impact was also deduced from negative correlations between supercooled liquid cloud fraction and dust amount globally [*Choi et al.*, 2010a; *Tan et al.*, 2014] and for East Asia [*Zhang et al.*, 2015]. *Min and Li* [2010] observed a strong enhancement of ice formation at warm temperatures during a Saharan dust outbreak over the eastern tropical Atlantic. By analysis of a large number of deep convective cloud systems

over China and adjacent regions, *Rosenfeld et al.* [2011] found dust-influenced clouds to have relatively high glaciation temperatures, along with clouds under influence of heavy air pollution. Model studies also report earlier or more pronounced glaciation if ice nucleating particle concentrations are increased [*van den Heever et al.*, 2006; *Diehl and Mitra*, 2015], but stress the complex and nonlinear feedbacks on further microphysical processes leading to precipitation formation, latent heat release and cloud dynamics [*van den Heever et al.*, 2006; *Ekman et al.*, 2007; *Paukert et al.*, 2017].

- In our simulations, we see a clear impact of ice multiplication via rime splintering, that is visible in both the in-cloud and the cloud top phase distribution. Its fingerprint is the reduction of the supercooled liquid fraction at temperatures between approximately -5 and -15°C. As the average reduction is only in the order of 10-20%, this does however not impact the derived cloud glaciation temperature. In contrast, *Rosenfeld et al.* [2011]'s analysis of convective cloud systems, maritime cloud exhibited the highest glaciation temperatures, and the authors attributed this to secondary ice formation processes occurring in these clouds. It is possible that other ice multiplication processes not included here could lead to a stronger impact and affect also the simulated cloud glaciation temperature. In any case, it seems advisable that for the detection of ice multiplication processes in observations, not only the cloud glaciation temperature T_{50} is analysed, but the entire cloud phase distribution wherever possible.
- Coarse-graining the simulation results from sub-km grid spacings to 1 to 3 km shifts the cloud top phase distribution to lower temperatures. In addition, the fingerprint of secondary ice formation in the binary cloud top pixel number fraction practically disappears. The reason for this effect is the lower contribution of ice cloud pixels compared to liquid cloud pixels to mass-weighted averages. If satellite retrievals implicitly include a similar weighting, this points to the need of very high resolution observations for the detection of such a signal from space. To date, only NPP/VIIRS (the Visible Infrared Imaging Radiometer Suite onboard the Suomi NPP (National Polar-orbiting Partnership) satellite) provides a cloud phase product available at sub-km resolution for the relevant cloud altitudes (nominally, 750 m resolution, or even 375 m if high-resolution channels are used [*Rosenfeld et al.*, 2014]). The resolution of the MODIS cloud products is 1 km, same as that of the CALIOP level 2 vertical feature mask in the upper troposphere [*Tan et al.*, 2014]. Long-term, gridded datasets from passive sensors have even coarser resolutions, e.g. the AVHRR-based Pathfinder

Atmospheres-Extended (PATMOS-X) dataset (1x4 km^2) [*Heidinger et al.*, 2014], or SEVIRI-based CLAAS-2 (3x3 km^2) [*Benas et al.*, 2017]. Note that the influence of vertical resolution has not been studied because of our focus on comparability to passive sensors measuring at visible and infrared wavelengths, but would be relevant for the comparison to active sensors, which provide vertically resolved phase information. Active radar sensors can also inform about larger, precipitating hydrometeors, which have been excluded from our analysis, but may exhibit a different phase partitioning behavior.

- No robust conclusions can be drawn at this point regarding the relative sensitivity of the cloud phase distribution to cloud dynamics and to microphysics. The two model setups, one more idealized, and strongly convective, and the other one more realistic, and with a less unstable profile, yielded qualitatively similar cloud phase distributions, which were however shifted by several K. But when the thermodynamic profile of the second setup was modified to give higher CAPE values, the binary cloud top phase distribution changed only little. This gives hope that microphysical sensitivities could be detected for ensembles of clouds, which form in similar but not identical thermodynamic conditions. If the conditions are too different, the resulting variability in the phase distribution is expected to dominate over the effect of different microphysical pathways, e.g. aerosol-induced heterogeneous freezing. We have not investigated the sensitivity to horizontal wind shear, which is also of importance for convective cloud development [e. g., *Fan et al.*, 2009].

In summary, our simulations show that while the cloud top phase distribution of deep convective clouds differs systematically from the in-cloud phase distribution, it still contains valuable information on microphysical processes such as the strength of primary and secondary ice formation. Future studies should address larger ensembles of clouds, more realistic model setups and the sensitivity to the choice of microphysical parameterizations. Furthermore, satellite simulators could help to derive the expected signal received by different sensors more exactly. The exploitation of passive satellite sensor information on cloud glaciation processes has to take into account the limitations due to resolution and co-variability of thermodynamic and aerosol conditions.

Acknowledgments

This project has received funding from the European Research Council (ERC) under the European Union's Horizon 2020 research and innovation programme under grant agreement No 714062 (ERC Starting Grant "C2Phase"). The COSMO simulation outputs of this study are freely available from the institutional repository KITopenData under doi:10.5445/IR/1000082997 in hourly time resolution. The data with the original time resolution are archived at the Steinbruch Centre for Computing at KIT and can be obtained from the authors upon request.

References

Baldauf, M., A. Seifert, J. Förstner, D. Majewski, M. Raschendorfer, and T. Reinhardt (2011), Operational convective-scale numerical weather prediction with the COSMO model: Description and sensitivities, *Monthly Weather Review*, *139*(12), 3887–3905, doi:10.1175/MWR-D-10-05013.1.

Benas, N., S. Finkensieper, M. Stengel, G.-J. van Zadelhoff, T. Hanschmann, R. Hollmann, and J. F. Meirink (2017), The MSG-SEVIRI-based cloud property data record CLAAS-2, *Earth System Science Data*, *9*(2), 415–434, doi:10.5194/essd-9-415-2017.

Bigg, E. K. (1953), The formation of atmospheric ice crystals by the freezing of droplets, *Q. J. Roy. Meteor. Soc.*, *79*(342), 510–519, doi:10.1002/qj.49707934207.

Carro-Calvo, L., C. Hoose, M. Stengel, and S. Salcedo-Sanz (2016), Cloud glaciation temperature estimation from passive remote sensing data with evolutionary computing, *Journal of Geophysical Research: Atmospheres*, *121*(22), 13,591–13,608, doi:10.1002/2016JD025552, 2016JD025552.

Cesana, G., and T. Storelvmo (2017), Improving climate projections by understanding how cloud phase affects radiation, *Journal of Geophysical Research: Atmospheres*, *122*(8), 4594–4599, doi:10.1002/2017JD026927, 2017JD026927.

Cesana, G., D. E. Waliser, X. Jiang, and J.-L. F. Li (2015), Multimodel evaluation of cloud phase transition using satellite and reanalysis data, *Journal of Geophysical Research: Atmospheres*, *120*(15), 7871–7892, doi:10.1002/2014JD022932, 2014JD022932.

Cesana, G., H. Chepfer, D. Winker, B. Getzewich, X. Cai, O. Jourdan, G. Mioche, H. Okamoto, Y. Hagihara, V. Noel, and M. Reverdy (2016), Using in situ airborne measurements to evaluate three cloud phase products derived from CALIPSO, *Journal of Geophysical Research: Atmospheres*, *121*(10), 5788–5808, doi:10.1002/2015JD024334, 2015JD024334.

Chepfer, H., P. Goloub, J. Spinhirne, P. H. Flamant, M. Lavorato, L. Sauvage, G. Brogniez, and J. Pelon (2000), Cirrus cloud properties derived from POLDER-1/ADEOS polarized radiances: First validation using a ground-based lidar network, *Journal of Applied Meteorology*, *39*(2), 154–168, doi:10.1175/1520-0450(2000)039<0154:CCPDFP>2.0.CO;2.

Choi, Y.-S., R. S. Lindzen, C.-H. Ho, and J. Kim (2010a), Space observations of cold-cloud phase change, *Proceedings of the National Academy of Sciences*, *107*(25), 11,211–11,216, doi:10.1073/pnas.1006241107.

Choi, Y.-S., C.-H. Ho, S.-W. Kim, and R. S. Lindzen (2010b), Observational diagnosis of cloud phase in the winter Antarctic atmosphere for parameterizations in climate models, *Advances in Atmospheric Sciences*, *27*(6), 1233–1245, doi:10.1007/s00376-010-9175-3.

Connolly, P. J., T. W. Choularton, M. W. Gallagher, K. N. Bower, M. J. Flynn, and J. A. Whiteway (2006), Cloud-resolving simulations of intense tropical Hector thunderstorms: Implications for aerosol-cloud interactions, *Quarterly Journal of the Royal Meteorological Society*, *132*(621C), 3079–3106, doi:10.1256/qj.05.86.

Cotton, R. J., and P. R. Field (2002), Ice nucleation characteristics of an isolated wave cloud, *Quarterly Journal of the Royal Meteorological Society*, *128*(585), 2417–2437, doi:10.1256/qj.01.150.

DeMott, P. J., A. J. Prenni, X. Liu, S. M. Kreidenweis, M. D. Petters, C. H. Twohy, M. S. Richardson, T. Eidhammer, and D. C. Rogers (2010), Predicting global atmospheric ice nuclei distributions and their impacts on climate, *P. Natl. Acad. Sci. USA*, *107*(25), 11,217–11,222.

Diehl, K., and S. K. Mitra (2015), New particle-dependent parameterizations of heterogeneous freezing processes: sensitivity studies of convective clouds with an air parcel model, *Atmospheric Chemistry and Physics*, *15*(22), 12,741–12,763, doi:10.5194/acp-15-12741-2015.

Ekman, A. M. L., A. Engström, and C. Wang (2007), The effect of aerosol composition and concentration on the development and anvil properties of a continental deep convective cloud, *Quarterly Journal of the Royal Meteorological Society*, *133*(627), 1439–1452, doi:10.1002/qj.108.

Fan, J., T. Yuan, J. M. Comstock, S. Ghan, A. Khain, L. R. Leung, Z. Li, V. J. Martins, and M. Ovchinnikov (2009), Dominant role by vertical wind shear in regulating aerosol effects on deep convective clouds, *Journal of Geophysical Research: Atmospheres*, *114*(D22), n/a–n/a, doi:10.1029/2009JD012352, d22206.

Fan, J., J. M. Comstock, and M. Ovchinnikov (2010), The cloud condensation nuclei and ice nuclei effects on tropical anvil characteristics and water vapor of the tropical tropopause layer, *Environmental Research Letters*, *5*(4), 044,005.

Fan, J., Y. Wang, D. Rosenfeld, and X. Liu (2016), Review of aerosol-cloud interactions: Mechanisms, significance, and challenges, *Journal of the Atmospheric Sciences*, *73*(11), 4221–4252, doi:10.1175/JAS-D-16-0037.1.

Field, P. R., R. P. Lawson, P. R. A. Brown, G. Lloyd, C. Westbrook, D. Moisseev, A. Miltenberger, A. Nenes, A. Blyth, T. Choularton, P. Connolly, J. Buehl, J. Crosier, Z. Cui, C. Dearden, P. DeMott, A. Flossmann, A. Heymsfield, Y. Huang, H. Kalesse, Z. A. Kanji, A. Korolev, A. Kirchgaessner, S. Lasher-Trapp, T. Leisner, G. McFarquhar, V. Phillips, J. Stith, and S. Sullivan (2017), Secondary ice production: Current state of the science and recommendations for the future, *Meteorological Monographs*, *58*, 7.1–7.20, doi:10.1175/AMSMONOGRAPHS-D-16-0014.1.

Findeisen, W. (1938), Die kolloidmeteorologischen Vorgänge bei der Niederschlagsbildung, *Meteorol. Zeitschr.*, *55*(4), 121–133.

Garrett, T. J., B. C. Navarro, C. H. Twohy, E. J. Jensen, D. G. Baumgardner, P. T. Bui, H. Gerber, R. L. Herman, A. J. Heymsfield, P. Lawson, P. Minnis, L. Nguyen, M. Poellot, S. K. Pope, F. P. J. Valero, and E. M. Weinstock (2005), Evolution of a Florida cirrus anvil, *Journal of the Atmospheric Sciences*, *62*(7), 2352–2372, doi:10.1175/JAS3495.1.

Hallett, J., and S. C. Mossop (1974), Production of secondary ice particles during the riming process, *Nature*, *249*(5452), 26–28.

Hande, L. B., and C. Hoose (2017), Partitioning the primary ice formation modes in large eddy simulations of mixed-phase clouds, *Atmospheric Chemistry and Physics*, *17*(22), 14,105–14,118, doi:10.5194/acp-17-14105-2017.

Hande, L. B., C. Hoose, and C. Barthlott (2017), Aerosol- and droplet-dependent contact freezing: Parameterization development and case study, *Journal of the Atmospheric Sciences*, *74*(7), 2229–2245, doi:10.1175/JAS-D-16-0313.1.

Heidinger, A. K., M. J. Foster, A. Walther, and X. T. Zhao (2014), The Pathfinder Atmospheres-Extended AVHRR climate dataset, *Bulletin of the American Meteorological Society*, *95*(6), 909–922, doi:10.1175/BAMS-D-12-00246.1.

Hiron, T., and A. I. Flossmann (2015), A study of the role of the parameterization of heterogeneous ice nucleation for the modeling of microphysics and precipitation of a convective cloud, *Journal of the Atmospheric Sciences*, *72*(9), 3322–3339, doi:10.1175/JAS-D-15-

0026.1.

Houze, R. A. (1993), *Cloud Dynamics*, *International Geophysics Series*, vol. 53, Academic Press, San Diego, USA and London, UK.

Hu, Y., S. Rodier, K.-m. Xu, W. Sun, J. Huang, B. Lin, P. Zhai, and D. Josset (2010), Occurrence, liquid water content, and fraction of supercooled water clouds from combined CALIOP/IIR/MODIS measurements, *Journal of Geophysical Research: Atmospheres*, *115*(D4), n/a–n/a, doi:10.1029/2009JD012384, d00H34.

Jäkel, E., M. Wendisch, T. C. Krisna, F. Ewald, T. Kölling, T. Jurkat, C. Voigt, M. A. Cecchini, L. A. T. Machado, A. Afchine, A. Costa, M. Krämer, M. O. Andreae, U. Pöschl, D. Rosenfeld, and T. Yuan (2017), Vertical distribution of the particle phase in tropical deep convective clouds as derived from cloud-side reflected solar radiation measurements, *Atmospheric Chemistry and Physics*, *17*(14), 9049–9066, doi:10.5194/acp-17-9049-2017.

Kanitz, T., P. Seifert, A. Ansmann, R. Engelmann, D. Althausen, C. Casiccia, and E. G. Rohwer (2011), Contrasting the impact of aerosols at northern and southern midlatitudes on heterogeneous ice formation, *Geophys. Res. Lett.*, *38*(L17802), doi: 10.1029/2011GL048532.

Kikuchi, M., H. Okamoto, K. Sato, K. Suzuki, G. Cesana, Y. Hagihara, N. Takahashi, T. Hayasaka, and R. Oki (2017), Development of algorithm for discriminating hydrometeor particle types with a synergistic use of CloudSat and CALIPSO, *Journal of Geophysical Research: Atmospheres*, *122*(20), 11,022–11,044, doi:10.1002/2017JD027113, 2017JD027113.

Komurcu, M., T. Storelvmo, I. Tan, U. Lohmann, Y. Yun, J. E. Penner, Y. Wang, X. Liu, and T. Takemura (2014), Intercomparison of the cloud water phase among global climate models, *Journal of Geophysical Research: Atmospheres*, *119*(6), 3372–3400, doi: 10.1002/2013JD021119, 2013JD021119.

Korolev, A. (2007), Limitations of the Wegener-Bergeron-Findeisen mechanism in the evolution of mixed-phase clouds, *J. Atmos. Sci.*, *64*, 3372–3375.

Korolev, A. V., G. A. Isaac, S. G. Cober, J. W. Strapp, and J. Hallett (2003), Microphysical characterization of mixed-phase clouds, *Q. J. Roy. Meteor. Soc.*, *129*, 39–65.

Lamb, D., and J. Verlinde (2011), *Physics and Chemistry of Clouds*, Cambridge University Press, Cambridge Books Online.

Liou, K.-N. (1981), Some aspects of the optical properties of ice clouds, in *Clouds their Formation, Optical Properties, and Effects*, edited by P. V. Hobbs and A. Deepak, pp. 315 –

354, Academic Press, doi:10.1016/B978-0-12-350720-4.50012-0.

Lohmann, U. (2017), Anthropogenic aerosol influences on mixed-phase clouds, *Current Climate Change Reports*, *3*(1), 32–44, doi:10.1007/s40641-017-0059-9.

Martins, J. V., A. Marshak, L. A. Remer, D. Rosenfeld, Y. J. Kaufman, R. Fernandez-Borda, I. Koren, A. L. Correia, V. Zubko, and P. Artaxo (2011), Remote sensing the vertical profile of cloud droplet effective radius, thermodynamic phase, and temperature, *Atmospheric Chemistry and Physics*, *11*(18), 9485–9501, doi:10.5194/acp-11-9485-2011.

Matus, A. V., and T. S. L'Ecuyer (2017), The role of cloud phase in Earth's radiation budget, *Journal of Geophysical Research: Atmospheres*, *122*(5), 2559–2578, doi: 10.1002/2016JD025951, 2016JD025951.

Mazin, I. P. (2006), Cloud phase structure: Experimental data analysis and parameterization, *Journal of the Atmospheric Sciences*, *63*(2), 667–681, doi:10.1175/JAS3660.1.

Min, Q., and R. Li (2010), Longwave indirect effect of mineral dusts on ice clouds, *Atmospheric Chemistry and Physics*, *10*(16), 7753–7761, doi:10.5194/acp-10-7753-2010.

Morrison, A. E., S. T. Siems, and M. J. Manton (2011), A three-year climatology of cloud-top phase over the Southern Ocean and North Pacific, *Journal of Climate*, *24*(9), 2405–2418, doi:10.1175/2010JCLI3842.1.

Morrison, H., and W. W. Grabowski (2008), Modeling supersaturation and subgrid-scale mixing with two-moment bulk warm microphysics, *Journal of the Atmospheric Sciences*, *65*(3), 792–812, doi:10.1175/2007JAS2374.1.

Mülmenstädt, J., O. Sourdeval, J. Delanoë, and J. Quaas (2015), Frequency of occurrence of rain from liquid-, mixed-, and ice-phase clouds derived from A-Train satellite retrievals, *Geophysical Research Letters*, *42*(15), 6502–6509, doi:10.1002/2015GL064604, 2015GL064604.

Murakami, M. (1990), Numerical Modeling of Dynamic and Microphysical Evolution of an Isolated Convective Cloud - The 19 July 1981 CCOPE Cloud, *Journal of the Meteorological Society of Japan*, *68*(2), 107–128.

Naud, C. M., and B. H. Kahn (2015), Thermodynamic phase and ice cloud properties in northern hemisphere winter extratropical cyclones observed by aqua airs, *Journal of Applied Meteorology and Climatology*, *54*(11), 2283–2303, doi:10.1175/JAMC-D-15-0045.1.

Naud, C. M., A. D. D. Genio, and M. Bauer (2006), Observational constraints on the cloud thermodynamic phase in midlatitude storms, *Journal of Climate*, *19*(20), 5273–5288, doi: 10.1175/JCLI3919.1.

Paukert, M., C. Hoose, and M. Simmel (2017), Redistribution of ice nuclei between cloud and rain droplets: Parameterization and application to deep convective clouds, *Journal of Advances in Modeling Earth Systems*, doi:10.1002/2016MS000841.

Pavolonis, M. J., A. K. Heidinger, and T. Uttal (2005), Daytime global cloud typing from avhrr and viirs: Algorithm description, validation, and comparisons, *Journal of Applied Meteorology*, *44*(6), 804–826, doi:10.1175/JAM2236.1.

Peng, J., H. Zhang, and Z. Li (2014), Temporal and spatial variations of global deep cloud systems based on cloudsat and calipso satellite observations, *Advances in Atmospheric Sciences*, *31*(3), 593–603, doi:10.1007/s00376-013-3055-6.

Petty, G. W. (2004), *A first course in atmospheric radiation*, Sundog Publishing, Madison, Wisconsin.

Pincus, R., S. Platnick, S. A. Ackerman, R. S. Hemler, and R. J. P. Hofmann (2012), Reconciling simulated and observed views of clouds: MODIS, ISCCP, and the limits of instrument simulators, *Journal of Climate*, *25*(13), 4699–4720, doi:10.1175/JCLI-D-11-00267.1.

Reisner, J., R. M. Rasmussen, and R. T. Bruintjes (1998), Explicit forecasting of supercooled liquid water in winter storms using the MM5 mesoscale model, *Quarterly Journal of the Royal Meteorological Society*, *124*(548), 1071–1107, doi:10.1002/qj.49712454804.

Rosenfeld, D., X. Yu, G. Liu, X. Xu, Y. Zhu, Z. Yue, J. Dai, Z. Dong, Y. Dong, and Y. Peng (2011), Glaciation temperatures of convective clouds ingesting desert dust, air pollution and smoke from forest fires, *Geophysical Research Letters*, *38*(21), n/a–n/a, doi: 10.1029/2011GL049423, l21804.

Rosenfeld, D., G. Liu, X. Yu, Y. Zhu, J. Dai, X. Xu, and Z. Yue (2014), High-resolution (375 m) cloud microstructure as seen from the NPP/VIIRS satellite imager, *Atmospheric Chemistry and Physics*, *14*(5), 2479–2496, doi:10.5194/acp-14-2479-2014.

Segal, Y., and A. Khain (2006), Dependence of droplet concentration on aerosol conditions in different cloud types: Application to droplet concentration parameterization of aerosol conditions, *Journal of Geophysical Research: Atmospheres*, *111*(D15), doi: 10.1029/2005JD006561, d15204.

Seifert, A., and K. D. Beheng (2006), A two-moment cloud microphysics parameterization for mixed-phase clouds. Part 1: Model description, *Meteorology and Atmospheric Physics*, *92*(1-2), 45–66.

Seifert, A., C. Köhler, and K. D. Beheng (2012), Aerosol-cloud-precipitation effects over Germany as simulated by a convective-scale numerical weather prediction model, *Atmospheric Chemistry and Physics*, *12*(2), 709–725, doi:10.5194/acp-12-709-2012.

Seifert, P., A. Ansmann, I. Mattis, U. Wandinger, M. Tesche, R. Engelmann, D. Müller, C. Pérez, and K. Haustein (2010), Saharan dust and heterogeneous ice formation: Eleven years of cloud observations at a central European EARLINET site, *J. Geophys. Res.*, *115*(D20201), doi:10.1029/2009JD013222.

Storelvmo, T. (2017), Aerosol effects on climate via mixed-phase and ice clouds, *Annual Review of Earth and Planetary Sciences*, *45*(1), 199–222, doi:10.1146/annurev-earth-060115-012240.

Storelvmo, T., and I. Tan (2015), The wegener-bergeron-findeisen process - its discovery and vital importance for weather and climate, *Meteorologische Zeitschrift*, *24*(4), 455–461, doi:10.1127/metz/2015/0626.

Sullivan, S. C., C. Hoose, and A. Nenes (), Investigating the contribution of secondary ice production to inâĂŘcloud ice crystal numbers, *Journal of Geophysical Research: Atmospheres*, *122*(17), 9391–9412, doi:10.1002/2017JD026546.

Tan, I., T. Storelvmo, and Y.-S. Choi (2014), Spaceborne lidar observations of the ice-nucleating potential of dust, polluted dust, and smoke aerosols in mixed-phase clouds, *Journal of Geophysical Research: Atmospheres*, *119*(11), 6653–6665, doi: 10.1002/2013JD021333.

Tao, W.-K., J.-P. Chen, Z. Li, C. Wang, and C. Zhang (2012), Impact of aerosols on convective clouds and precipitation, *Reviews of Geophysics*, *50*(2), n/a–n/a, doi: 10.1029/2011RG000369, rG2001.

Taylor, S., P. Stier, B. White, S. Finkensieper, and M. Stengel (2017), Evaluating the diurnal cycle in cloud top temperature from SEVIRI, *Atmospheric Chemistry and Physics*, *17*(11), 7035–7053, doi:10.5194/acp-17-7035-2017.

van den Heever, S. C., G. G. Carrió, W. R. Cotton, P. J. DeMott, and A. J. Prenni (2006), Impacts of nucleating aerosol on florida storms. Part I: Mesoscale simulations, *Journal of the Atmospheric Sciences*, *63*(7), 1752–1775, doi:10.1175/JAS3713.1.

Weidle, F., and H. Wernli (2008), Comparison of ERA40 cloud top phase with POLDER-1 observations, *Journal of Geophysical Research: Atmospheres*, *113*(D5), n/a–n/a, doi: 10.1029/2007JD009234, d05209.

Weisman, M. L., and J. B. Klemp (1982), The dependence of numerically simulated convective storms on vertical wind shear and buoyancy, *Mon. Wea. Rev.*, *110*, 504–520, doi: 10.1175/1520-0493(1982)110<0504:TDONSC>2.0.CO;2.

Weisman, M. L., and R. Rotunno (2000), The use of vertical wind shear versus helicity in interpreting supercell dynamics, *Journal of the Atmospheric Sciences*, *57*(9), 1452–1472, doi:10.1175/1520-0469(2000)057<1452:TUOVWS>2.0.CO;2.

Winker, D. M., J. Pelon, J. A. C. Jr., S. A. Ackerman, R. J. Charlson, P. R. Colarco, P. Flamant, Q. Fu, R. M. Hoff, C. Kittaka, T. L. Kubar, H. L. Treut, M. P. Mccormick, G. Mégie, L. Poole, K. Powell, C. Trepte, M. A. Vaughan, and B. A. Wielicki (2010), The CALIPSO mission, *Bulletin of the American Meteorological Society*, *91*(9), 1211–1230, doi: 10.1175/2010BAMS3009.1.

Yuan, T., and Z. Li (2010), General macro- and microphysical properties of deep convective clouds as observed by MODIS, *Journal of Climate*, *23*(13), 3457–3473, doi: 10.1175/2009JCLI3136.1.

Yuan, T., J. V. Martins, Z. Li, and L. A. Remer (2010), Estimating glaciation temperature of deep convective clouds with remote sensing data, *Geophysical Research Letters*, *37*(8), n/a–n/a, doi:10.1029/2010GL042753, l08808.

Zeng, Y., U. Blahak, and D. Jerger (2016), An efficient modular volume-scanning radar forward operator for NWP models: description and coupling to the COSMO model, *Quarterly Journal of the Royal Meteorological Society*, *142*(701), 3234–3256, doi: 10.1002/qj.2904.

Zhang, D., D. Liu, T. Luo, Z. Wang, and Y. Yin (2015), Aerosol impacts on cloud thermodynamic phase change over East Asia observed with CALIPSO and CloudSat measurements, *Journal of Geophysical Research: Atmospheres*, *120*(4), 1490–1501, doi: 10.1002/2014JD022630, 2014JD022630.

Zipser, E. J. (2003), Some views on “hot towers” after 50 years of tropical field programs and two years of TRMM data, *Meteorological Monographs*, *51*, 49–58, doi:10.1175/0065-9401(2003)029<0049:CSVOHT>2.0.CO;2.

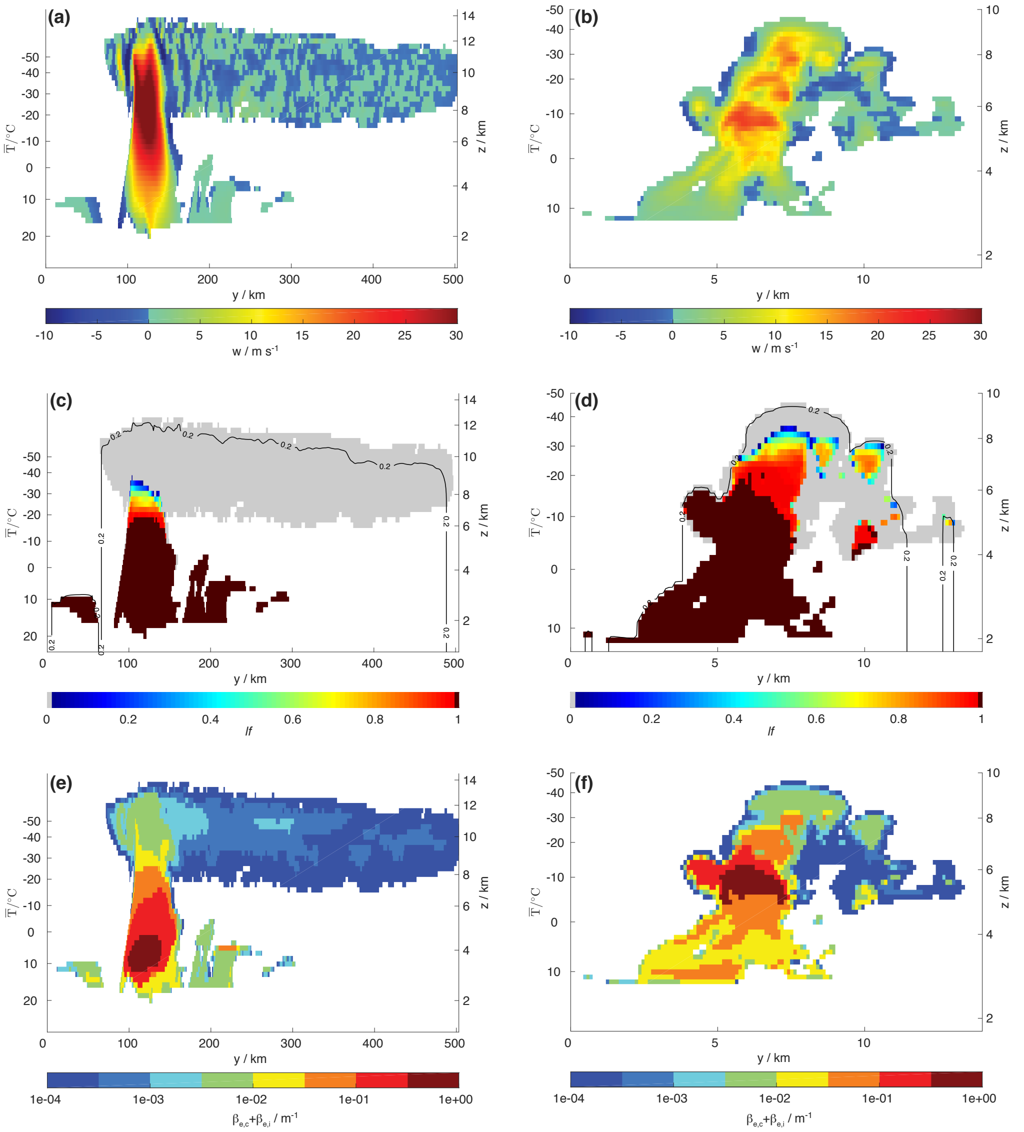

232 **Figure 1.** East-west cross sections through the main updraft of the simulated clouds. Left column: warm bubble simulations at 3 h from model start, right column: semi-idealized simulations at 2 h 48 min from model start. (a) and (b): vertical velocity, (c) and (d): liquid mass fraction lf (color shading) and a contour of an optical depth of 0.2 (integrated from cloud top), (e) and (f): shortwave extinction coefficient. The temperature axis is based on domain-average temperatures for each altitude level and is therefore not accurate within the clouds. The color shading is only plotted for pixels with condensate mass $q_c + q_i > 10^{-8}$ kg/kg.

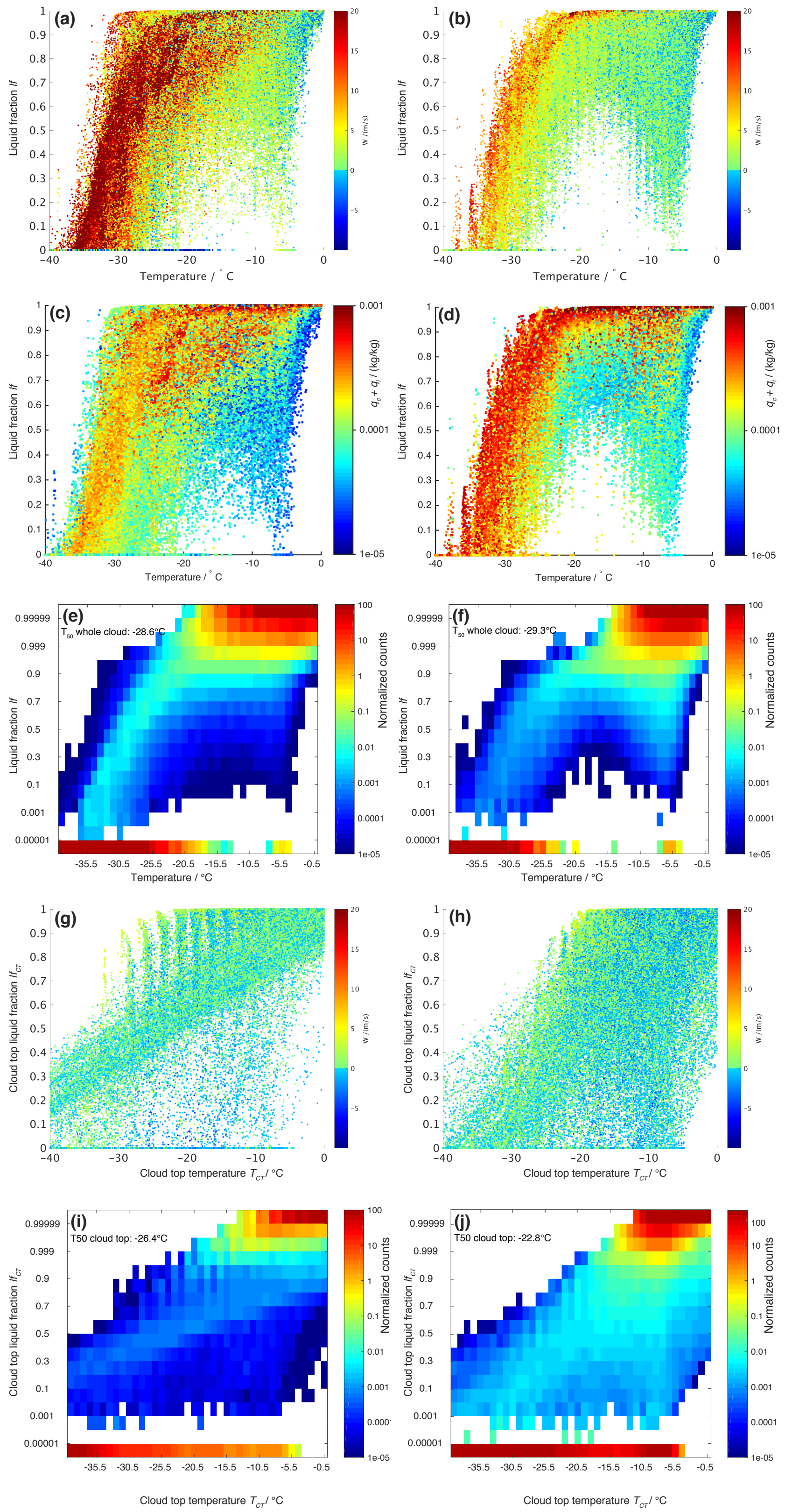

Figure 2. In-cloud and cloud top liquid fraction. Left column: warm bubble simulations, right column: semi-idealized simulations. (a), (b), (c) and (d): pixelwise in-cloud liquid fraction; (e) and (f): normalized 2D histograms of the in-cloud liquid fraction vs temperature ($N/(\Delta T \Delta lf N_{tot})$); (g) and (h): pixelwise cloud top liquid fraction; (i) and (j): normalized 2D histograms of the cloud top liquid fraction vs temperature ($N/(\Delta T \Delta lf_{CT} N_{tot,CT})$). Note the nonlinear y-axes in (e), (f), (i) and (j).

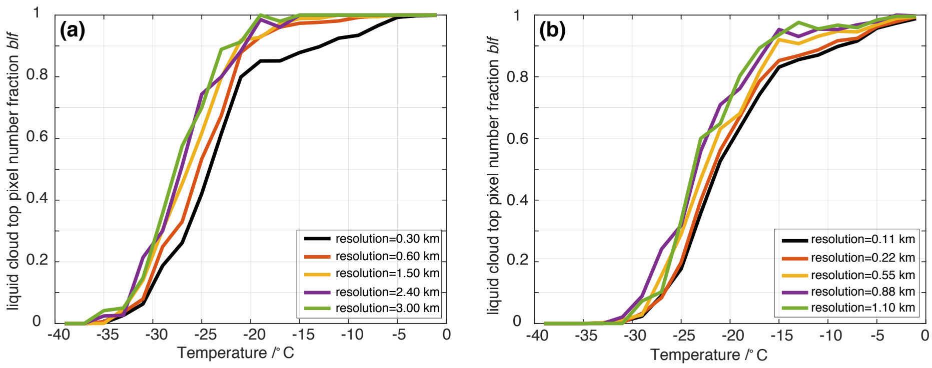

Figure 3. Binary liquid cloud top pixel number fraction for original model grid (black lines) and different degrees of coarse graining (colored lines). (a) warm bubble simulation, (b) semi-idealized simulation.

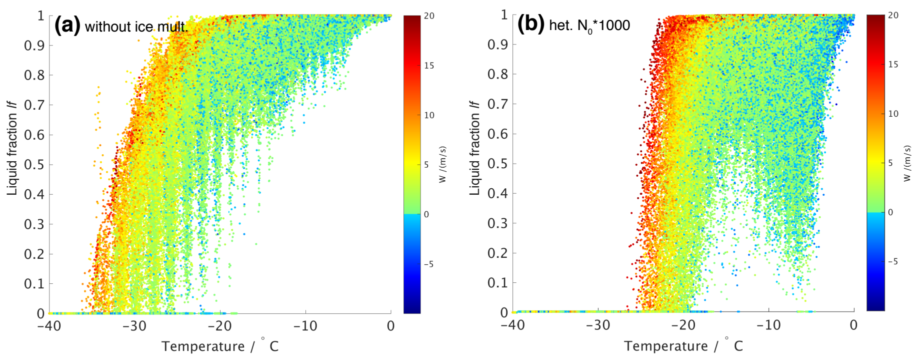

Figure 4. In-cloud liquid mass fraction ((a) and (b)) for sensitivity experiments in the semi-idealized setup.

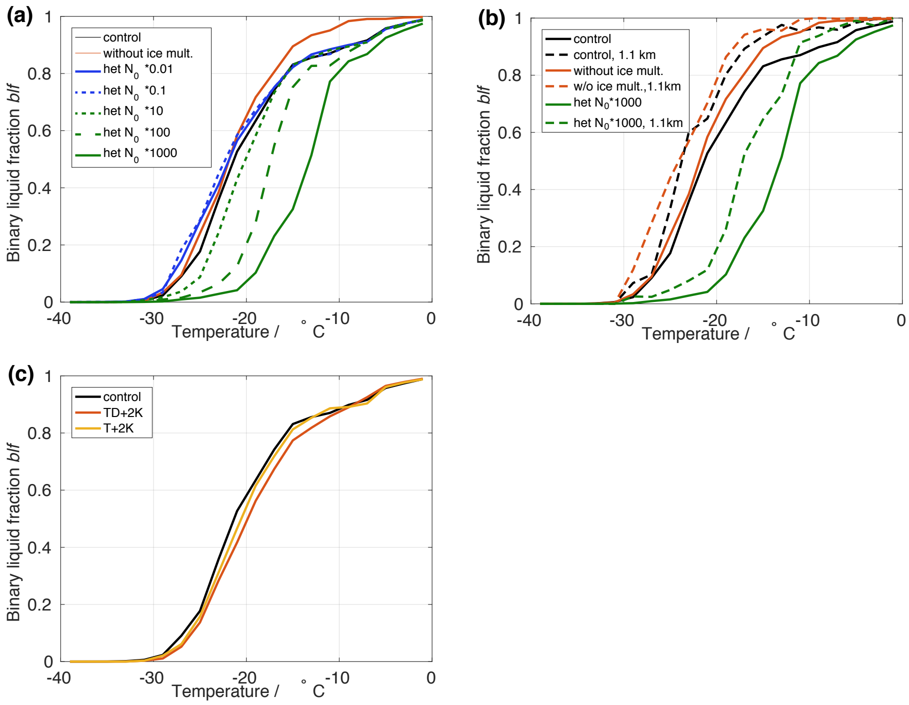

Figure 5. Binary liquid cloud top pixel number fractions for the sensitivity experiments for the semi-idealized setup. (a) Control run and the sensitivity simulations with scaled ice nucleation and without ice multiplication. (b) Comparison of results on the original model grid (110 m resolution) and diagnosed on a 1.1 km grid. (c) Sensitivity experiments (110 m resolution) with modified input thermodynamic profiles: increases of near-surface temperature T and dew point temperature TD.